Geyman, E.C., and Maloof, A.C., 2021, Facies control on carbonate $\delta^{13}C$ on the Great Bahama Bank: Geology, v. 49, https://doi.org/10.1130/G48862.1

Facies control on carbonate $\delta^{13}C$ on the Great Bahama Bank

Emily C. Geyman[1], Adam C. Maloof[1]

[1]Department of Geosciences, Princeton University, Princeton, NJ 08544

SUPPLEMENTAL MATERIAL

1. Detailed Methods

Stable isotope analysis of carbonate sediments. All $\delta^{13}C$ and $\delta^{18}O$ measurements were made at Princeton University. Carbonate sediments were rinsed 3x in deionized water, dried, homogenized using mortar and pestle, and then placed in individual borosilicate reaction vessels. Algal carbonate grains were scraped from the specimens in the field and then treated with 30% H_2O_2 for 12 hours to remove residual organic matter before being rinsed 3x in deionized water (Wierzbowski, 2007; Figure S1). All samples were heated to 110°C to remove volatiles, capped and flushed with He to remove atmospheric gas from the reaction vessels, and finally reacted at 72°C in a GasBench II preparation device coupled to a Sercon continuous flow isotope ratio mass spectrometer. The precision and accuracy of $\delta^{13}C$ and $\delta^{18}O$ measurements was monitored through analysis of 15 standards for every 57 measured samples. $\delta^{13}C$ and $\delta^{18}O$ data are reported in the standard delta notation relative to Vienna Pee Dee Belemnite (VPDB). Average precision is <0.1‰ (1σ) for $\delta^{13}C$ and <0.2‰ (1σ) for $\delta^{18}O$.

Measurements of total dissolved inorganic carbon (DIC) and $\delta^{13}C$ of DIC. All water samples were filtered through a 0.2 μm filter at the time of sampling in the field and stored in a dark cooler until chemical analysis. Total dissolved inorganic carbon (DIC) and $\delta^{13}C$ of DIC were measured at the Light Stable Isotope Mass Spec Lab at the University of Florida.

DIC was measured using a UIC (Coulometrics) 5014 CO_2 coulometer coupled with an AutoMate automated carbonate preparation device. Approximately 5 ml of sample was weighed into septum top tubes and placed into the AutoMate carousel. Acid and CO_2-free nitrogen carrier gas was then injected into the sample vial through a double needle assembly and evolved CO_2 was carried through a silver nitrate scrubber to the coulometer where total C was measured. Replicate analysis indicates that the uncertainty (1σ) is 3.66 μmol kg^{-1}.

Carbon isotopic ratios of DIC were measured with a Thermo Finnigan DeltaPlus XL isotope ratio mass spectrometer with a GasBench II universal on-line gas preparation device. Water was injected into septum top vials containing 0.5 ml phosphoric acid and filled with helium. The

acidification releases all DIC into the headspace and the mixture of CO_2 and He are sampled by the GasBench II. All isotope results are reported in standard delta notation relative to Vienna Pee Dee Belemnite (VPDB).

Sample processing: sieving of grain size fractions and identification of carbonate constituents

Sediment samples (*Main text*, Fig. 1) were sorted through a stack of 63 µm, 125 µm, 250 µm, 500 µm, and 1000 µm sieves. Samples were collected during two field seasons (June 2017 and June 2018), but the 250 µm sieve was only used for the 2018 season. Grains from the coarse fractions (e.g., >500 µm and >1000 µm) were picked and placed on 8x8 grid slides (Figure S1a) to be imaged using a stereomicroscope before $\delta^{13}C/\delta^{18}O$ analysis. The grid slide images (Figure S1a) provide a record to document and verify carbonate grain type (ooid, grapestone, coated grain, gastropod, bivalve, etc.) associated with each isotopic measurement. Aliquots of the sieved grain size fractions were homogenized using mortar and pestle and analyzed for $\delta^{13}C/\delta^{18}O$.

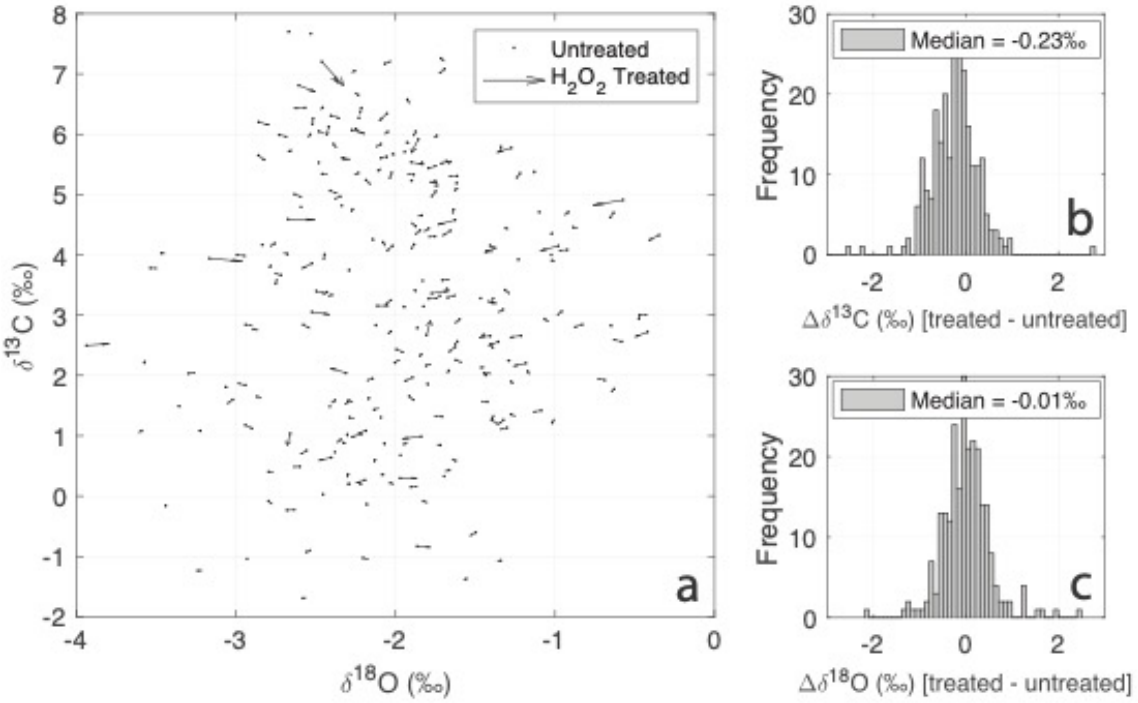

Figure S1: An experiment demonstrating that the H_2O_2 pre-treatment for removing organic matter from the calcareous green algae specimens (Figure S2b; Wierzbowski, 2007) does not significantly alter the measured $\delta^{13}C$ and $\delta^{18}O$ values. (a) We selected a random subset of 245 algae and separated the powders into two aliquots. On one aliquot, we measured the $\delta^{13}C$ and $\delta^{18}O$ values without H_2O_2 treatment. On the other aliquot, we measured the $\delta^{13}C$ and $\delta^{18}O$ values after letting the sample react with 30% H_2O_2 for 12 hours. The scatter plot in (a) shows the $\delta^{18}O$-$\delta^{13}C$ of the untreated samples as dots. The arrows point to the $\delta^{18}O$-$\delta^{13}C$ of the corresponding treated samples. (b-c) The median offset between treated and untreated samples is -0.23‰ and -0.01‰ for $\delta^{13}C$ and $\delta^{18}O$, respectively.

Figure S2: (a) An 8x8 grid slide (1 cm divisions) containing carbonate grains (primarily benthic foraminifera, gastropods, and grapestones) analyzed for $\delta^{13}C$. (b) A specimen of *Halimeda* (calcareous green algae) with multiple calcified petals analyzed for $\delta^{13}C$.

2. Carbonate constituents

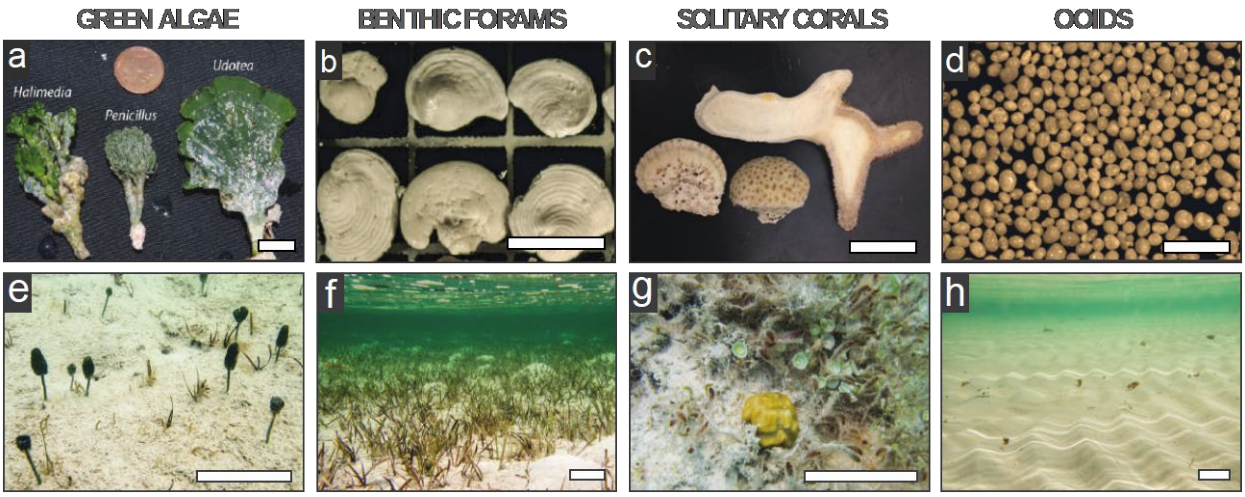

Figure S3: (a) calcifying green algae (*Halimeda, Penicillus, Udotea*), (b) benthic foraminifera (*Peneroplis*), (c,g) small corals (*Porites, Siderastrea, Manicina*), and (d) ooids from NWA. The photos in (e-h) illustrate typical sedimentary environments associated with the carbonate types in (a-d). Scale bar is 1 cm in (a-d) and ~10 cm in (e-h).

Figure S3 illustrates four of the abundant carbonate constituents in NWA (calcifying green algae, benthic foraminifera, corals, and ooids) and typical sedimentary environments associated with each of those four carbonate types. Other carbonate constituents in *Main text*, Fig. 1e that require additional explanation include:

1. *Lithified Holocene ooid aeolianite* – coastal pinstriped oolite outcrops at Joulters Cays (Halley & Harris, 1979).
2. *Weakly lithified subtidal crusts* – partially cemented sediments below current mean sea level (MSL) and co-mingling with unconsolidated Holocene sediment. Distinguished from (6) by their partial degree of cementation/lithification.
3. *Beachrock* – Figure S4 illustrates an example of beachrock (partially cemented intertidal to supratidal sediment) in outcrop and hand sample. We use the term "beachrock" after Shinn (2009) and others.
4. *Bivalves & gastropods (beach)* – Figure S5 shows a shell beach representing this category. Note that these subaerially-exposed bivalve and gastropod shells tend to have lower $\delta^{13}C$ than their subtidal equivalents (*Main text*, Fig. 1e).
5. *Lithified 10-130 ka sediments: subaerial* – Figure S6 shows three representative samples from this category. The term *subaerial* refers to their *current* location (i.e., above MSL today), rather than the environment at the time they were deposited. This category encompasses both coral reef facies and aeolianites (Figure S5). Where possible, we microdrilled the hand samples, targeting both individual carbonate grains (shell fragments, ooids, and coated grains) and cements. The $\delta^{13}C$ distributions of these two sub-populations are shown in *Main text*, Fig. 1e.
6. *Lithified 10-130 ka sediments: subtidal* – recrystallized Eemian sediments lying below current MSL, accessed in places where the Holocene unconsolidated sediment cover is relatively thin (e.g., <30 cm, denoted as squares in *Main text*, Fig. 1a).
7. *Cave carbonate (<130 ka)* – Figure S7 shows a representative cave carbonate sample, microdrilled for $\delta^{13}C$ across the sequential layers of the speleothem. All samples in the *Cave carbonate* category were collected from Morgan's Cave (coordinates: UTM 17N 799901, 2788063).

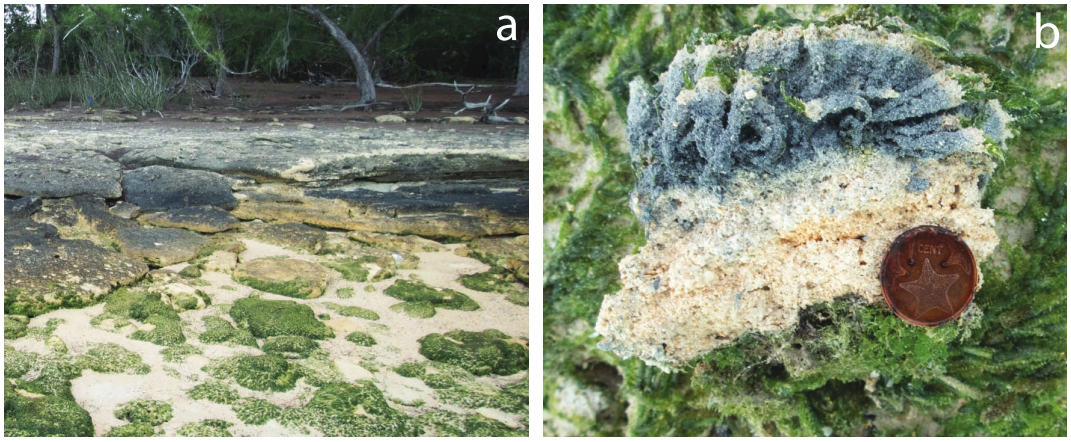

Figure S4: "Beachrock" in outcrop (a) and hand sample (b). Notice the *Batophora* algae growing on the beachrock. The Bahamian penny is 1.7 cm in diameter.

Figure S5: An example of *cerithid* gastropod and *Geloina* bivalve shells subaerially exposed on the beach. Hammer is ~34 cm long.

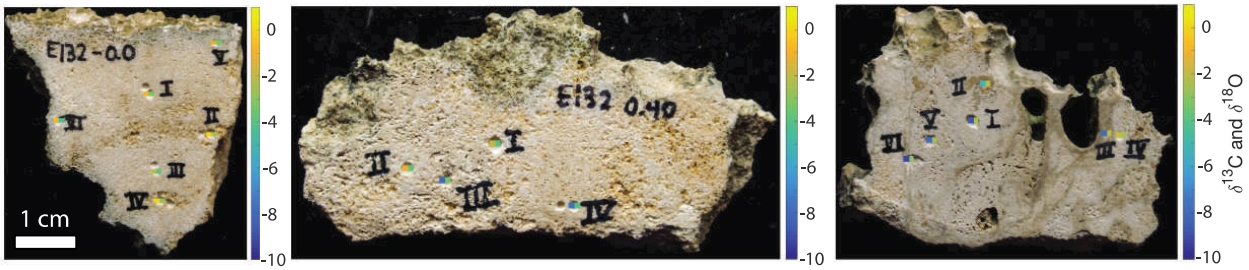

Figure S6: Three representative samples from Morgan's Bluff, which hosts a succession of Eemian coral reef to aeolianite strata (coordinates: UTM 17N 799899, 2788061, 0-8 masl). These samples fall into the category "*Lithified 10-130 ka sediments: subaerial"* in *Main text*, Fig. 1e. The samples are microdrilled for $\delta^{18}O$ and $\delta^{13}C$: the square on the left records $\delta^{18}O$ and the square on the right records $\delta^{13}C$.

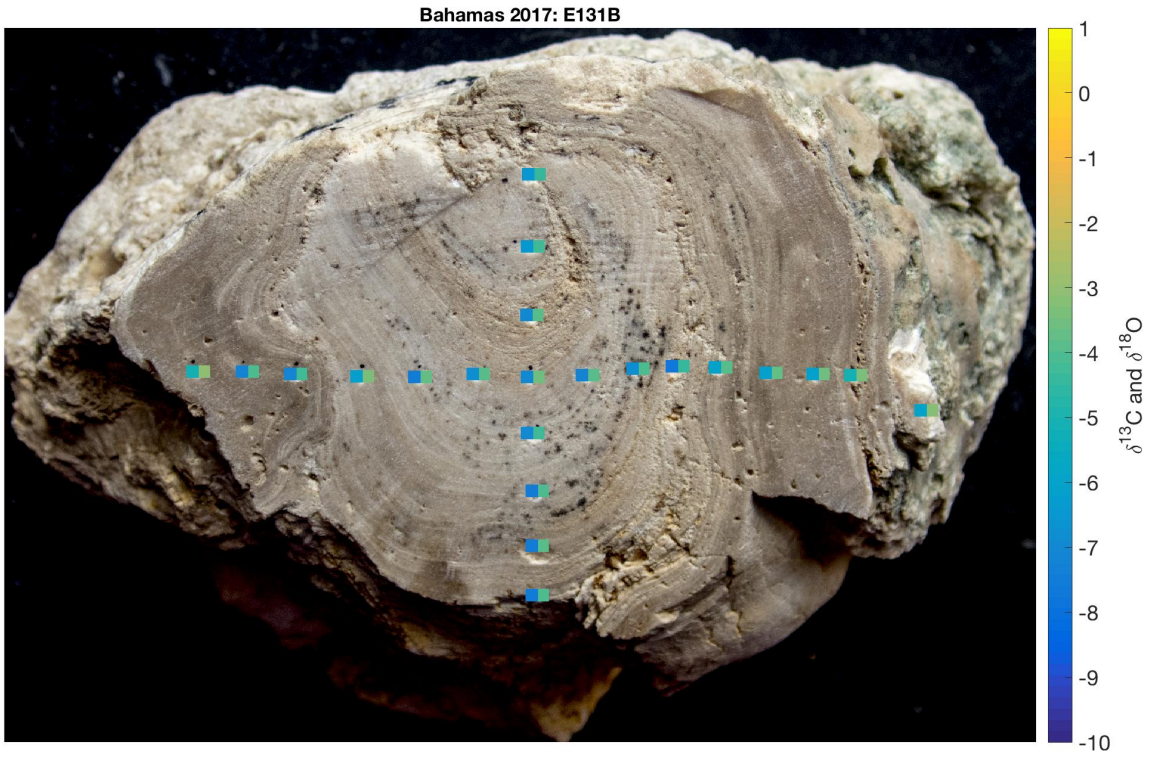

Figure S7: Cave carbonate sample from Morgan's Cave (coordinates: UTM 17N 799901, 2788063), microdrilled for $\delta^{13}C$ and $\delta^{18}O$: the square on the left records $\delta^{13}C$ and the square on the right records $\delta^{18}O$.

Sampling $\delta^{13}C$ across the Eemian-Holocene parasequence boundary

Main text, Fig. 4b provides a cartoon illustration of NWA geology in order to highlight the types of locations where we could sample $\delta^{13}C$ across the Eemian-Holocene parasequence boundary (Fig. 4a). These are the locations where recent storm erosion has made the Holocene sedimentary cover relatively thin (e.g., <30 cm). Figure S8 shows an example of such a site.

3. Measuring size-fraction-specific $\delta^{13}C$ compositions

In addition to measuring the $\delta^{13}C$ composition of homogenized bulk sediment, we measured the $\delta^{13}C$ of each grain size fraction (<63, 63-125, 125-500, 500-1000, >1000 μm) (see section 1). Since many sediments lack measurable quantities of some of the size fractions (i.e., no <63 μm mud-sized particles in sediments collected from grainstone shoals), the number of $\delta^{13}C$ measurements for each grain size varies, from 174 to 257 (Figure S9).

To obtain complete maps of the $\delta^{13}C$ of each size fraction across the study area, we must estimate $\delta^{13}C$ in regions for which we have no direct measurements (Figure S9). We take a probabilistic approach. For each pixel location in the map area, we generate a probability

distribution of the estimated $\delta^{13}C$, where *all* samples of the appropriate size fraction contribute a vote to the estimated $\delta^{13}C$ composition, but each sample's vote is weighted by the inverse square distance between that sample's location and the pixel of interest. As a result, at pixel locations that are far from all sampling sites, all of the samples in our dataset contribute approximately equally to the $\delta^{13}C$ probability distribution (since they have similar inverse square distances to the pixel of interest). The resulting $\delta^{13}C$ probability distribution has a mean and spread approaching that computed for the unweighted dataset. In contrast, at pixel locations that are near one or more sampling sites, the $\delta^{13}C$ probability distribution will be dominated by those local observations. Figure S10 illustrates the generation of these $\delta^{13}C$ probability distributions for each pixel in the map area by summing individual gaussian-distributed "votes" from our library of sediment samples. Figure S9 shows the spatial patterns in the resulting $\delta^{13}C$ estimates and the associated uncertainties.

Figure S8: An example of one of the sites on west Andros (24.854642, -78.254797) where recent storm erosion has removed much of the Holocene unconsolidated sediment cover, providing a window into the underlying Eemian sedimentary rock. Imagery from Google Earth.

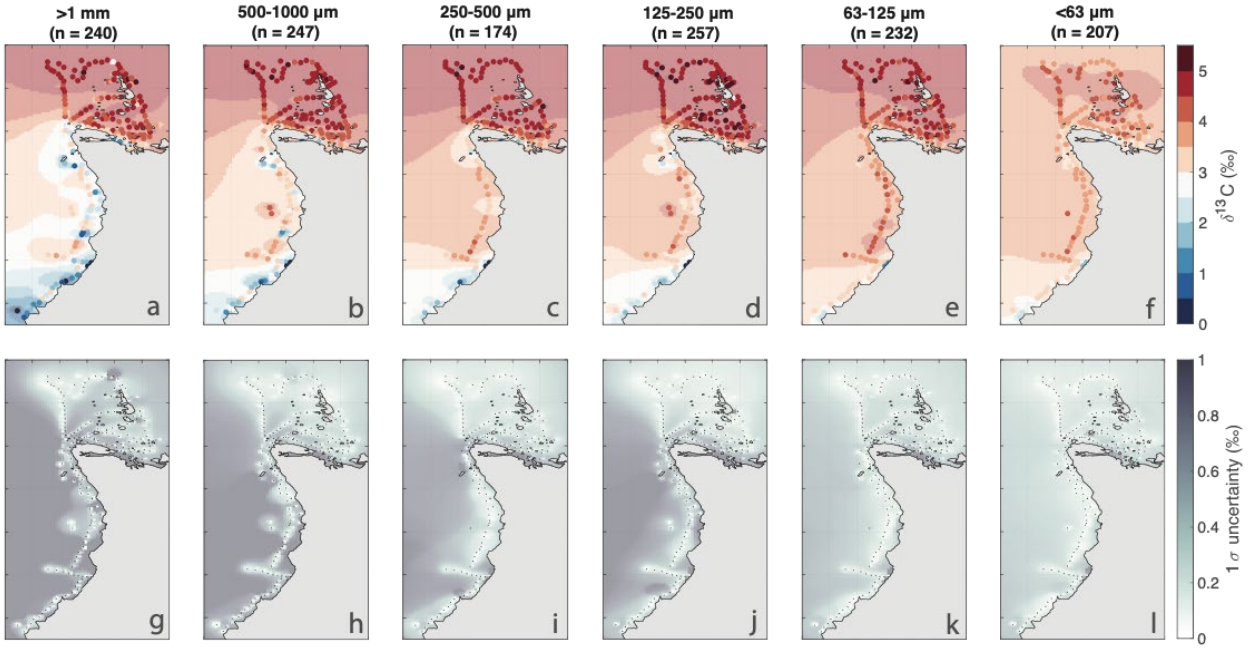

Figure S9: (a-f) The $\delta^{13}C$ compositions of six grain size fractions (<63, 63-125, 125-500, 500-1000, >1000 µm) sieved from the bulk sediment. The dots show the $\delta^{13}C$ at sampling locations, and the contoured backgrounds (partly transparent, to distinguish from the dots) show *estimated* $\delta^{13}C$ in regions where we did not collect samples. The estimation procedure is illustrated in Figure S10. (g-l) The reported uncertainty of the pixelwise $\delta^{13}C$ estimate is based on the spread of the $\delta^{13}C$ probability distributions computed for each pixel (see Figure 10). Specifically, we report the uncertainty as ½ the spread of the middle 68% of the pixelwise $\delta^{13}C$ probability distributions (Figure S10), which is analogous to 1σ for a normal distribution. Note in (g-l) that the uncertainty approaches the analytical $\delta^{13}C$ uncertainty (<0.1‰) near the sample locations, and approaches ~1‰ far from any sample sites. The uncertainty is greatest for the >1 mm size fraction (g), which shows substantial cross-platform variability (a), and least for the <63 µm size fraction (l), which maintains roughly constant $\delta^{13}C$ across the study area (f).

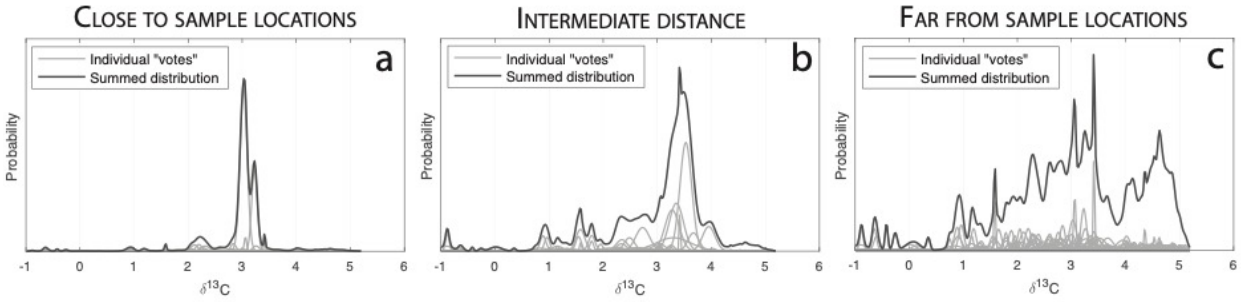

Figure S10: An illustration of our methodology for estimating $\delta^{13}C$ (and associated uncertainty) for each size fraction at the locations in the study area for which we have no samples (Figure

S9). (a-c) Every $\delta^{13}C$ measurement for the appropriate size fraction ($n \approx 200$) contributes a vote to the $\delta^{13}C$ distribution. Each vote has the form of a Gaussian distribution, with a mean equal to the measured $\delta^{13}C$ value and a standard deviation equal to the 1σ analytical uncertainty (~0.1‰) of the measurement. However, the "weight" of each vote (the integrated area of the Gaussian distribution) varies according to the inverse squared distance between the sample location and the location of the pixel for which we are estimating $\delta^{13}C$. Samples collected close to the pixel of interest are given more weight than more distant samples. As a result, for pixel locations that are close to one or a few sample locations, only a few "votes" dominate the $\delta^{13}C$ distribution (a). (b-c) At locations that are more distant from sample locations, the $n \approx 200$ "votes" contribute more equally, causing the spread of the summed $\delta^{13}C$ distribution to increase.

4. Leveraging grain size measurements and facies map to generate spatial estimates of banktop $\delta^{13}C$

Grain size analysis

We measured the grain size distribution of each sediment sample using a Beckman Coulter LS 13 320 Laser Diffraction Particle Size Analyzer (LDPSA) with the Universal Liquid Module. The LDPSA measures the relative volume of each grain size in 117 bins from 0.4 μm to 2000 μm. In total, we measured the grain size spectra of 363 sediment samples from NWA. Principal component analysis (PCA) for dimensionality reduction followed by *k*-means unsupervised clustering of the 363 spectra yields quantitative grain size classifications for the sediment samples that closely align with the Dunham (1962) classes of mudstone, wackestone, packstone, oolitic grainstone, and shelly grainstone (Figure S11, Geyman et al., 2021). These *k*-means classifications closely align with our qualitative Dunham classifications made in the field at each site. From the grain size spectra in Figure S11, we can compute the relative proportions of each of our sieved grain size fractions (<63, 63-125, 125-500, 500-1000, >1000 μm) in the five facies categories.

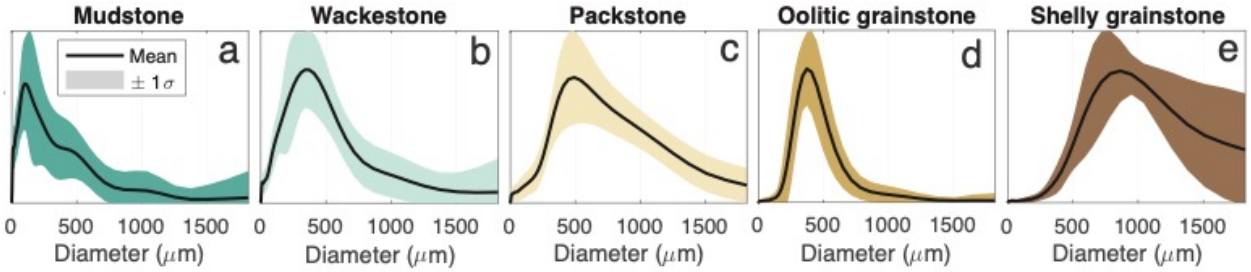

Figure S11: Representative grain size spectra of mudstone, wackestone, packstone, oolitic grainstone, and shelly grainstone facies on NWA. The spectra in (a-e) represent the five centroids of the *k*-means unsupervised clustering of our 363 grain size spectra (Geyman et al., 2021).

We can re-combine our $\delta^{13}C$ measurements of each size fraction (Figure S9) in weighted averages based on Figure S11 to estimate the bulk $\delta^{13}C$ composition of a sediment sample for any given facies. We use the facies map of Geyman et al. (2021) to determine which weighted average (Figure S11) to use for each pixel location on the study area. Figure S12 shows the resulting $\delta^{13}C$ map, which gives our best estimate of the bulk $\delta^{13}C$ composition of the modern banktop, accounting for spatial trends in the $\delta^{13}C$ of each size fraction (Figure S9) as well as the variable contribution of each grain size as governed by the local sedimentary facies.

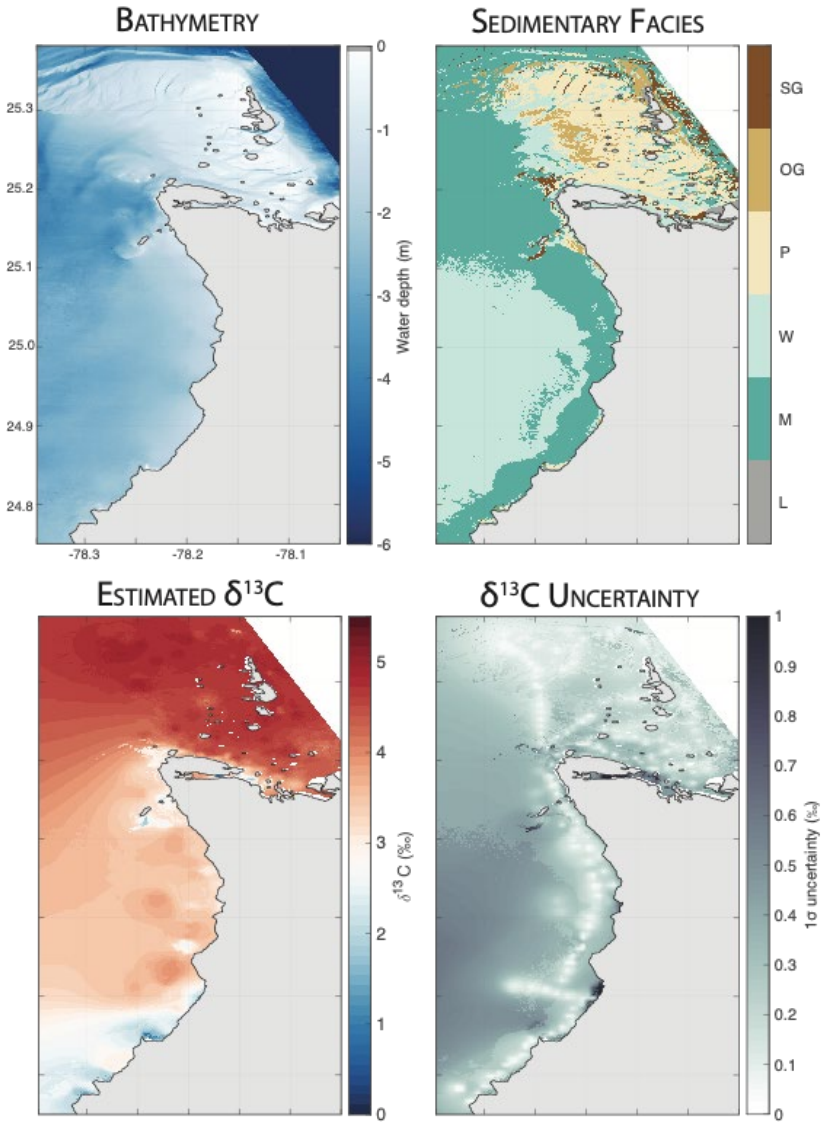

Figure S12: Maps of water depth, sedimentary facies, estimated bulk sediment $\delta^{13}C$, and uncertainty in the $\delta^{13}C$ estimate. Bathymetry from Geyman & Maloof (2019) and facies map from Geyman et al. (2021). The map of $\delta^{13}C$ uncertainty propagates the individual uncertainty estimates for each sediment size fraction (Figure S9).

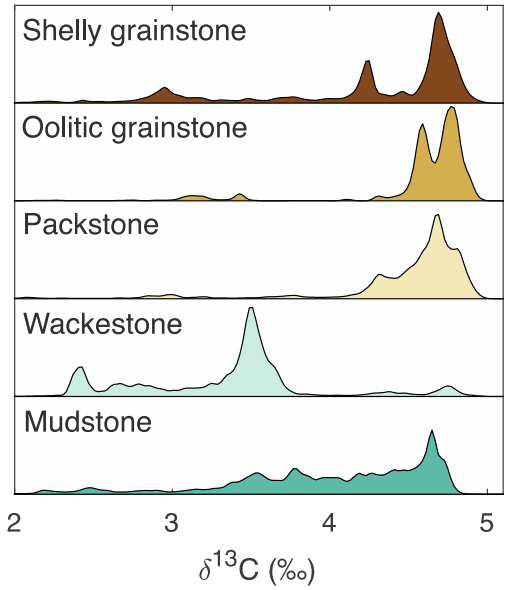

Figure S13: $\delta^{13}C$ distributions for each facies computed from the maps in Figure S13.

5. Estimating parasequence-scale $\delta^{13}C$ changes

To estimate the extent to which the $\delta^{13}C$ variability in Figure S12 might get incorporated in meter-scale parasequences, we use the methodology of Geyman et al. (2021) to generate parasequences by sampling the facies and $\delta^{13}C$ maps (Figure S12) in random walks and directed walks up the steepest-average gradient towards land (i.e., shallowing-upwards). We use a modified Walther's Law approach, whereby the local water depth modulates deposition and erosion. Moving to deeper water corresponds to an erosive event that removes previously-deposited stratigraphy. See Geyman et al. (2021) for a detailed description of the methodology. Figures S14-15 illustrate examples of shallowing-upwards parasequences and Figure S16 illustrates examples of stochastic (random walk) parasequences.

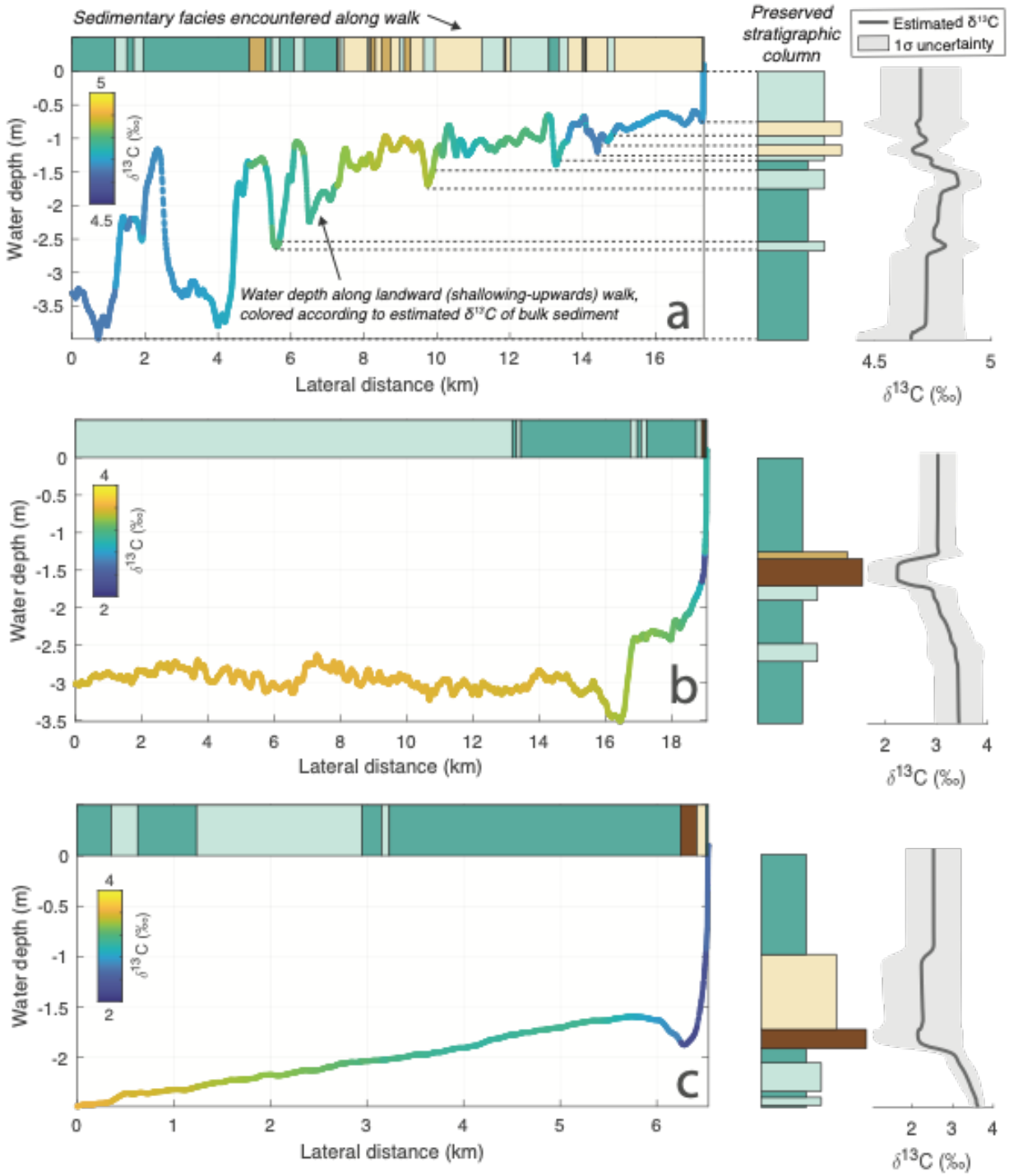

Figure S14: An illustration of the generation of shallowing-upwards parasequences by laterally sampling the facies, bathymetry, $\delta^{13}C$, and $\delta^{13}C$ uncertainty maps in Figure S12.

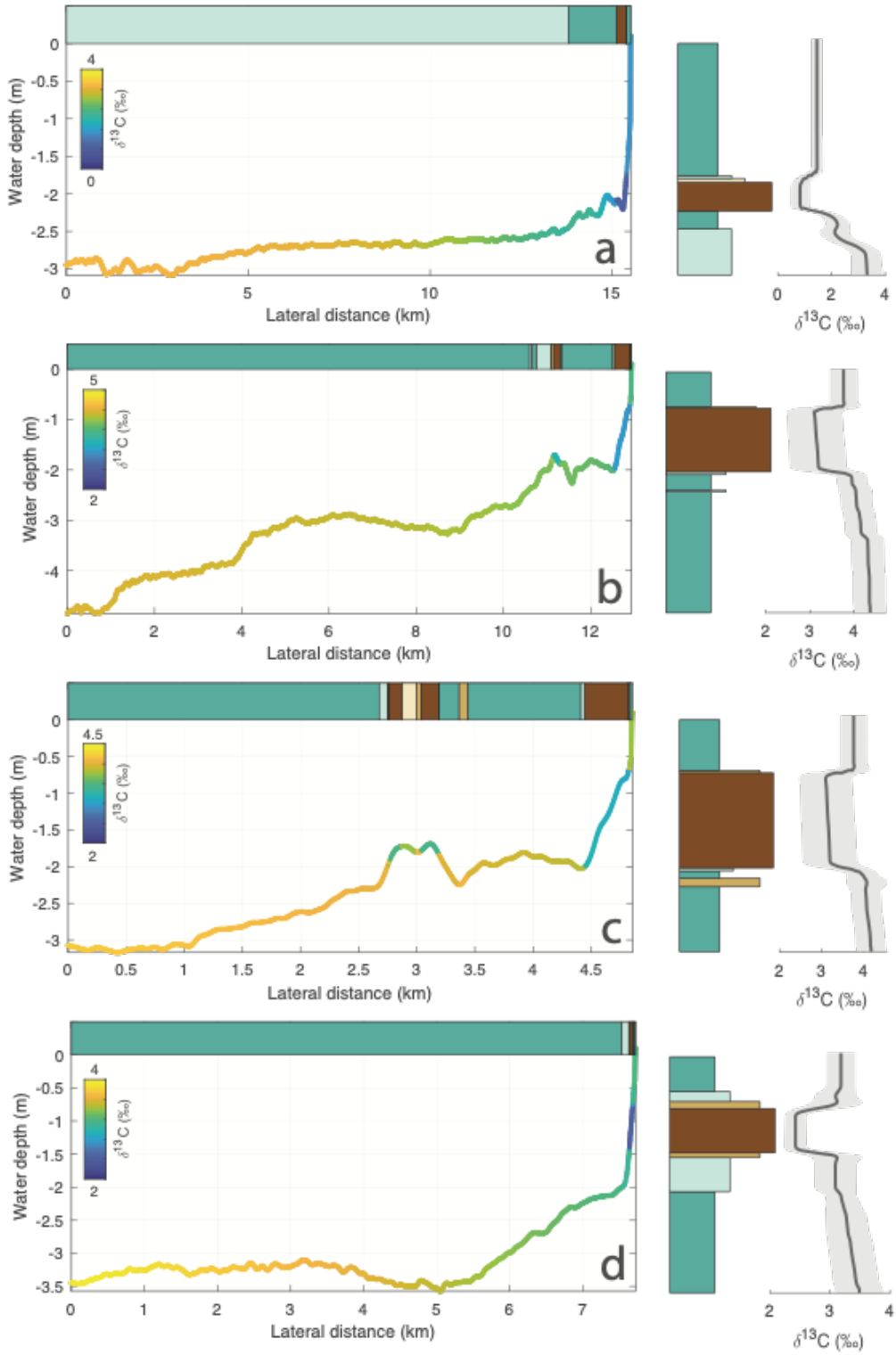

Figure S15: Four shallowing-upwards parasequences that illustrate how facies-imposed $\delta^{13}C$ shifts get superimposed on longer-wavelength $\delta^{13}C$ trends in the simulated stratigraphic columns. In particular, in (a-d), the transition from mudstone/wackestone to grainstone typically corresponds to a ~1‰ reduction in $\delta^{13}C$.

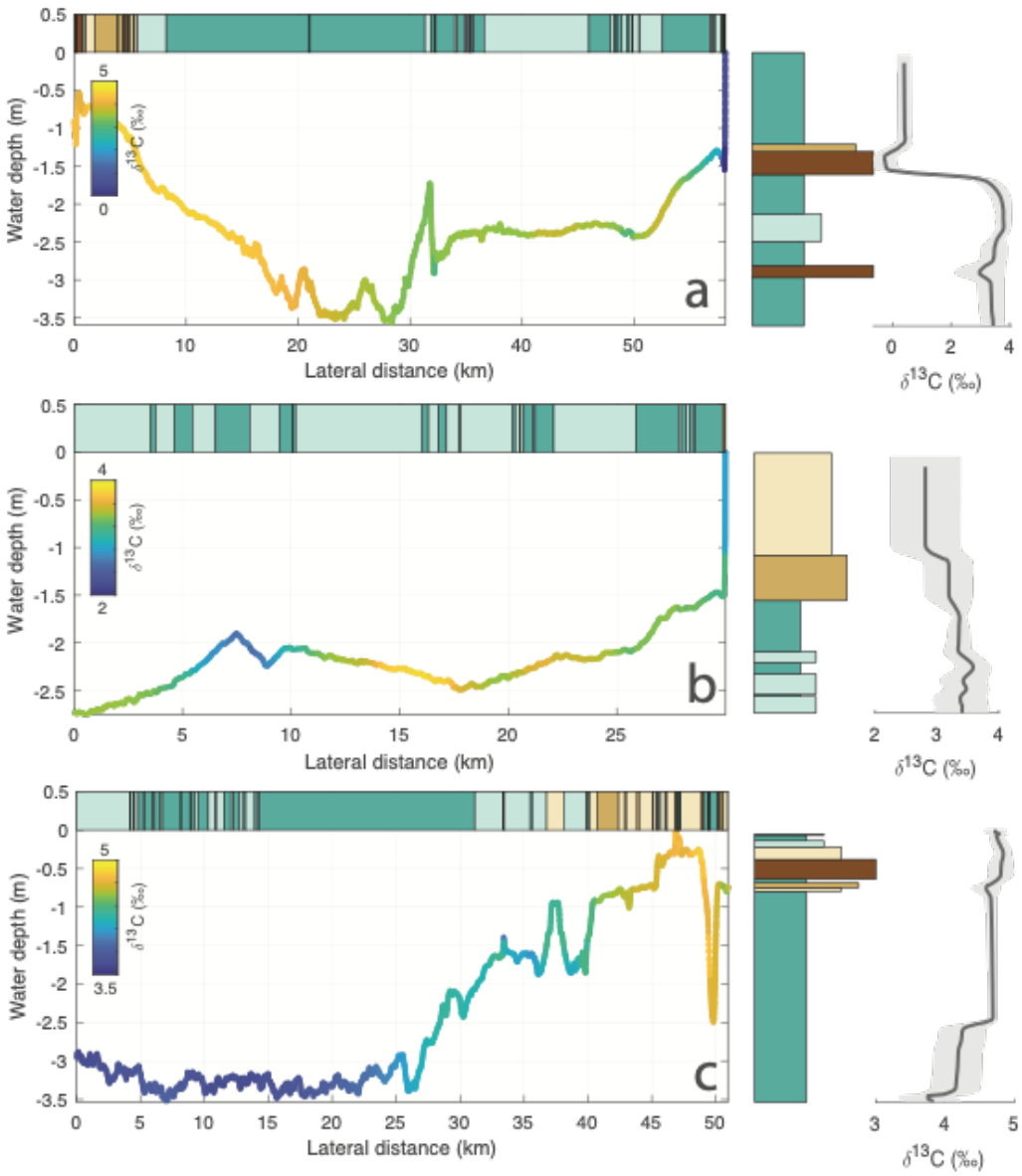

Figure S16: An illustration of the generation of stochastic (random walk) parasequences by laterally sampling the facies, bathymetry, $\delta^{13}C$, and $\delta^{13}C$ uncertainty maps in Figure S12.

6. Cross-shelf gradient in $\delta^{13}C$ of DIC

In the *Main text*, we suggest that the ~5‰ gradient in $\delta^{13}C$ of DIC (Fig. S17a) is driven by the addition of remineralized terrestrial organic carbon (Patterson & Walter, 1994), primarily from the mangrove ponds and tidal channels dominating the coastline of west Andros (Figure S19c). Support for this hypothesis comes from combined seawater [DIC], $\delta^{13}C$ of DIC, $\delta^{18}O$, and δD measurements. Broadly, from the shelf edge to interior, [DIC] declines due to carbonate precipitation (Figure S17b). However, seawater samples from nearshore west Andros record an

increase in [DIC] (Fig. S17c, Fig. S18b). This increase in [DIC] is associated with a reduction in $\delta^{13}C$ of DIC (Fig. S17c) and occurs in relatively 'evolved' banktop waters (based on their progress along the $\delta^{18}O$ vs. δD evaporative enrichment trajectory – Fig. S18a). We interpret this coupled reduction in $\delta^{13}C$ of DIC and increase in [DIC] as reflecting the addition of remineralized organic carbon (Fig. S17c) sourced from the tidal flats of west Andros.

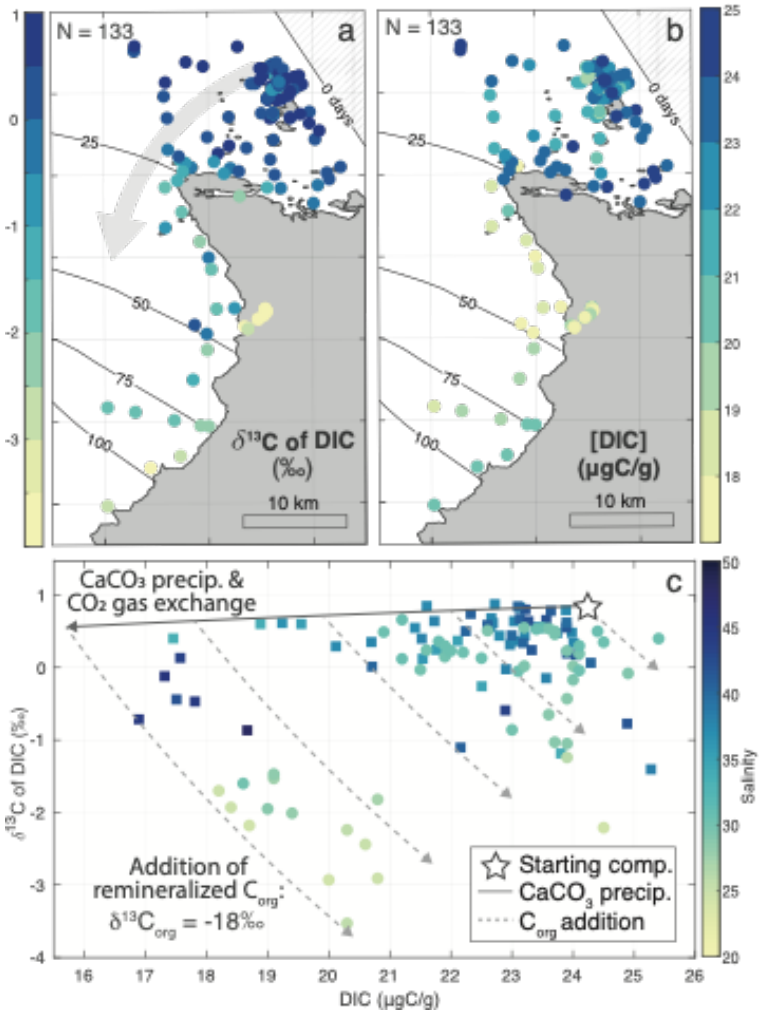

Figure S17: Spatial trends in (a) $\delta^{13}C$ of DIC and (b) [DIC]. Contours represent banktop water ages (in days) based on the ^{14}C measurements of Broecker & Takahashi (1966). (c) The paired [DIC] and $\delta^{13}C$ of DIC data are well-described by a combination of (1) carbonate precipitation and gas exchange and (2) the addition of remineralized organic carbon, which simultaneously increases [DIC] and lowers $\delta^{13}C$ of DIC and salinity. Coupled carbonate precipitation and CO_2 gas exchange leads to little change in the $\delta^{13}C$ of DIC, because the depletion in ^{13}C of residual DIC caused by the precipitation of ^{13}C-enriched carbonate is mostly offset by the enriching-effect of CO_2 gas escape (ε = -10‰; Siegenthaler & Munnich, 1981) (Geyman & Maloof, 2019). Waters become most depleted in $\delta^{13}C$ when they reach the tidal creeks of west Andros (Figure S19c).

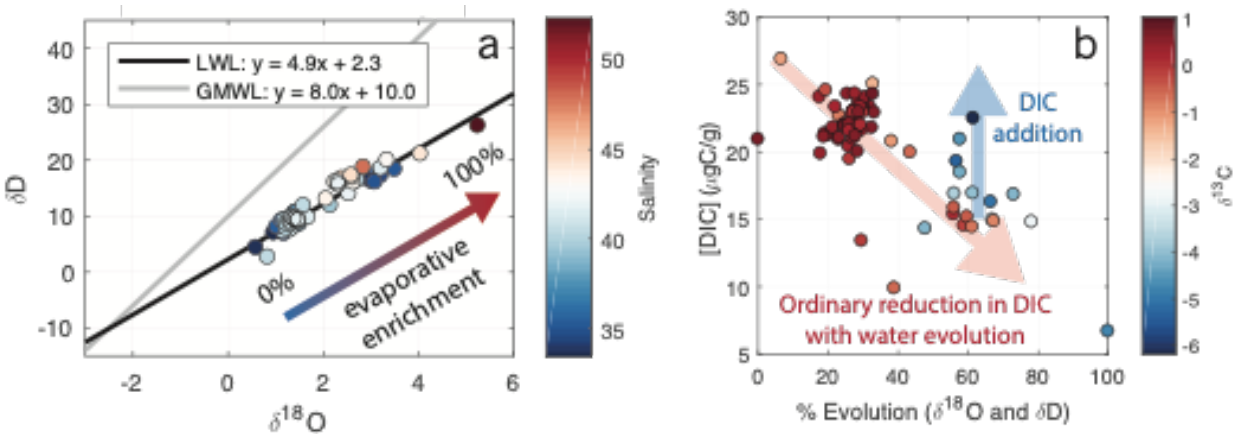

Figure S18: Banktop waters follow an evaporative enrichment trajectory in the space of $\delta^{18}O$ vs. δD. The slope of the local water line (LWL, +4.9) is consistent with evaporative slopes (Gibson et al. 2008). GMWL is the *global meteoric water line* (Craig, 1961; Dansgaard, 1964}. (b) The coupled increase in DIC and reduction in $\delta^{13}C$ of DIC observed in Figure S17 typically occurs in relatively evolved banktop waters (e.g., those that have traversed the evaporative enrichment trajectory in (a) by roughly 60%). Panel (b) suggests a situation in which banktop waters to the north of Andros Island, where there are no significant terrestrial fluxes, maintain a high $\delta^{13}C$. Once the waters reach the west coast of Andros (after roughly 25-50 days, based on the Broecker & Takahashi (1966) ^{14}C water ages—*Main text,* Fig. 2) they mix with isotopically-light, DIC-rich waters fluxing out of the tidal channels.

Main text Fig. 2d illustrates that the depleted $\delta^{13}C$ of DIC values we observe along west Andros represent a primarily *nearshore* phenomenon. Figure S19 shows that the same is true for bulk sediment $\delta^{13}C$. The $\delta^{13}C$ measurements of Swart et al. (2009), taken farther from land, display consistent values of 4.5-5.5‰. Bulk sediment $\delta^{13}C$ values only decline within 5-10 km of the coast of west Andros (Fig. S19a).

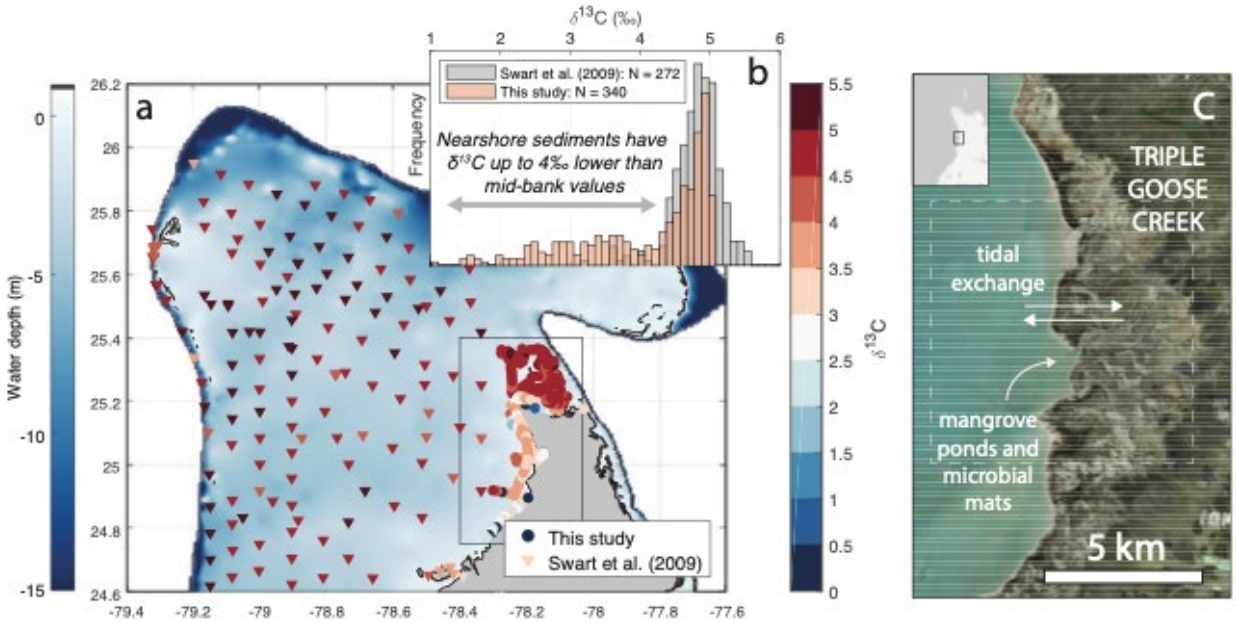

Figure S19: The northern portion of the Great Bahama Bank (GBB), with bulk sediment $\delta^{13}C$ measurement from Swart et al. (2009) and this study. Background bathymetry from Harris et al. (2015). (b) Both Swart et al. (2009) and this study observe sediments with a $\delta^{13}C$ composition in the range 4.5-5.5‰. However, nearshore sediments from this study exhibit $\delta^{13}C$ dropping as low as 0-1‰. (c) Triple Goose Creek is the largest complex of tidal channels on the northwest coast of Andros Island, although the entire length of the coastline is punctuated by tidal channels that exchange water between the banktop and the shallow inland ponds that support mangrove and microbial mat communities (Maloof & Grotzinger, 2012).

References

Broecker, W. & Takahashi, T., 1966. Calcium carbonate precipitation on the Bahama Banks, *Journal of Geophysical Research*, 71(6), 1575–1602.

Craig, H., 1961. Isotopic variations in meteoric waters, *Science*, 133(3465), 1702–1703.

Dansgaard, W., 1964. Stable isotopes in precipitation, *Tellus*, 16(4), 436–468.

Dunham, R.J., 1962. Classification of carbonate rocks according to depositional texture. *AAPG: Classification of Carbonate Rocks‐A Symposium*, 108‐121.

Geyman, E.C. & Maloof, A.C., 2019. A simple method for extracting water depth from multispectral satellite imagery in regions of variable bottom type. *Earth and Space Science* 6, 527‐537 (2019).

Geyman, E.C., Maloof, A.C., and Dyer, B. How is sea level change encoded in carbonate stratigraphy? *Earth and Planetary Science Letters, accepted*. 2021.

Gibson, J. J., Birks, S. J., & Edwards, T. W. D., 2008. Global prediction of δ_A and δ^2H- $\delta^{18}O$ evaporation slopes for lakes and soil water accounting for seasonality, *Global Biogeochemical Cycles*, 22(2).

Halley, R. B., & Harris, P. M. (1979). Fresh-water cementation of a 1,000-year-old oolite. *Journal of Sedimentary Research*, 49(3), 969‐987.

Harris, P. M. M., Purkis, S. J., Ellis, J., Swart, P. K., & Reijmer, J. J. G., 2015. Mapping bathymetry and depositional facies on Great Bahama Bank, *Sedimentology*, 62(2), 566‐589.

Maloof, A. C. & Grotzinger, J. P., 2012. The Holocene shallowing-upward parasequence of north-west Andros Island, Bahamas, *Sedimentology*, 59, 1375‐1407.

Patterson, W. & Walter, L., 1994. Depletion of ^{13}C in seawater DIC on modern carbonate platforms: significance for the carbon isotopic record of carbonates, *Geology*, 22(2), 885–888.

Shinn, E.A. (2009) The mystique of beachrock. In: Perspectives in Carbonate Geology (Eds P. Swart, G. Eberli and J. McKenzie), *Int. Assoc. Sed. Spec. Publ.*, 41, 19‐28. Wiley-Blackwell, West Sussex, UK.

Siegenthaler, U. & Munnich, K. 1981. $^{13}C/^{12}C$ fractionation during CO_2 transfer from air to sea. In: *Carbon Cycle Modeling: SCOPE 16*, B. Bolin, Ed. John Wiley & Sons, 249‐257.

Swart, P., Reijmer, J., & Otto, R., 2009. A re-evaluation of facies on Great Bahama Bank II: variations in the $\delta^{13}C$, $\delta^{18}O$ and mineralogy of surface sediments, *Int. Assoc. Sedimentol. Spec. Publ.*, 41, 47–59.

Wierzbowski, H., 2007. Effects of pre-treatments and organic matter on oxygen and carbon isotope analyses of skeletal and inorganic calcium carbonate, *International Journal of Mass Spectrometry*, 268, 16-29.